Beam scattering and heating at the front of an electron beam injected into a plasma

L. Y. Chan[a] and R. L. Stenzel
Department of Physics, University of California, Los Angeles, California 90024

(Received 21 December 1993; accepted 17 February 1994)

A dense pulsed electron beam ($t_r \leqslant 20$ ns, $V_b = 200$ V, $i_b \leqslant 2$ A, $n_b/n_e \leqslant 10\%$) is injected into a uniform magnetoplasma ($n_e = 1 - 4 \times 10^{10}$ cm^{-3}, $kT_e \leqslant 0.5$ eV, $B_0 = 90$ G) to study wave–particle interactions that occur at the front of the beam on short-time scales during which the ions are regarded as fixed and immobile. Above a threshold beam density ($n_b/n_e > 5\%$), the beam front is observed using optical diagnostics to rapidly erode due to beam scattering and energetic tail production, and broaden into a warm front that propagates slower than its injected speed. Using radio-frequency (RF) antennas, the beam is observed to bunch due to the streaming beam–plasma instability and create a ballistic beam mode ($f_B = nf_{pe}$), which collapses into broadband electrostatic turbulence during the onset of beam scattering. A low-frequency electrostatic wave mode ($f_{pi} < f_{\mathrm{LF}} < f_{pe}$) is also detected that is coupled to the scattering process. These measurements show that rich beam–plasma phenomena occur in this electron time-scale regime, which are not adequately addressed by current plasma theory.

I. INTRODUCTION

The study of the propagation of short pulsed electron beams into plasmas is of interest in several areas of plasma and beam physics. In space physics, pulsed electron beams have been injected into the ionosphere for remote probing of the magnetosphere.[1] Relativistic electron beams (REB) have been injected into gas and plasma[2,3] to develop high-power microwave and x-ray sources, and to study plasma accelerator concepts.[4] In most experimental investigations of beam propagation, the ion dynamics plays an essential role in the beam–plasma interactions and propagation dynamics. In contrast, we study in this experiment[5] a novel regime of electron beam propagation where ion processes are not important due to the short beam pulses and fast beam diagnostics used. Moreover, conditions at the beam front produce new transient beam–plasma phenomena that are absent in steady-state beam–plasmas.

Whelan and Stenzel[6] have investigated the generation of electromagnetic radiation due to the injection of electron beams in plasmas, however their diagnostics could not resolve phenomena on the time scale of the beam front. Michel and Hogge[7] have developed an energy analyzer to study electron beam propagation through turbulent plasmas. Several one-dimensional simulations[8,9] have involved the injection of an electron beam into a plasma, and Pritchett and Winglee[10] have done two-dimensional electrostatic simulations of the injection of beams into space plasmas. However, none of these simulations report results that are similar to the observations of our experiment. There have also been a few theoretical studies that consider transient effects in the beam–plasma instability at the front of the electron beam pulse.[11,12]

The main result of this experiment is that beam scattering and production of energetic electron tails can occur without ion dynamics. We observe that the beam bunches strongly due to the streaming beam–plasma instability and then collapses into broadband turbulence, accompanied by beam scattering and energetic tail production. In most beam–plasma interactions, Langmuir wave collapse or ion wave scattering are used to explain the production of energetic tail electrons. Such ion mechanisms develop too slowly in our experiment to be significant and implies that current plasma theory may not adequately explain the beam–plasma interactions observed in this novel beam propagation regime. The organization of this paper is as follows. The experimental setup and diagnostics techniques are described in Sec. II. Then the basic optical measurements, with beam scattering and front erosion results, are presented in Sec. III. Electrostatic antenna measurements of beam bunching and concurrent optical and wave measurements are shown in Sec. IV. Finally, our conclusions are summarized in Sec. V.

II. EXPERIMENTAL SETUP

The experiment is performed in a cylindrical vacuum chamber, 30 cm in diameter and 150 cm in length, which has a uniform magnetic field of 90 G along its axis produced by external solenoidal coils. A rotary pump and diffusion pump are used to produce a base pressure of 1×10^{-6} Torr, and argon is maintained in the chamber at pressures of $2-4 \times 10^{-4}$ Torr. Figure 1 shows the experimental setup of the source cathodes and diagnostic probes. Two barium oxide-coated cathodes are used, so that the electron beam and background plasma parameters may be varied independently. The main cathode creates a pulsed plasma discharge, then during the afterglow of this discharge, the beam cathode injects an electron beam ($V_b = 200$ V, $i_b \leqslant 2$ A) into a quiescent plasma ($n_e = 1 - 4 \times 10^{10}$ cm^{-3}, $kT_e \leqslant 0.5$ eV). The plasma sheath in front of the beam cathode acts as an anode, while a grounded annular plate is used to define the beam diameter and to provide a coaxial return current path for the injected beam. The beam impedance is matched to 50 Ω

---

[a] Present address: Laser Plasma Branch, Plasma Physics Division, U.S. Naval Research Laboratory, Washington, D.C. 20375.

1070-664X/94/1(6)/2063/9/$6.00

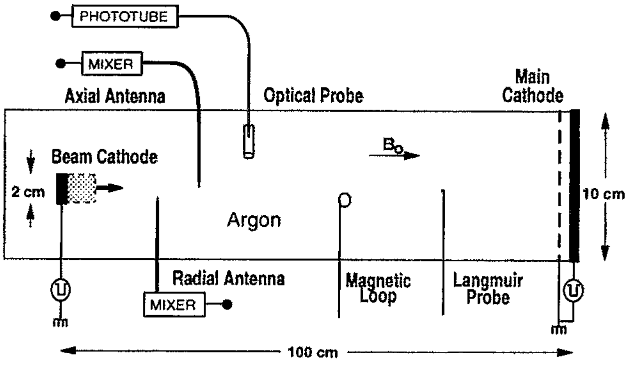

FIG. 1. Experimental setup for injecting an electron beam into a magnetized afterglow plasma and measuring the propagation of the beam front into the plasma.

TABLE I. Basic experimental and physical parameters.

Neutral pressure (Argon)	$P_0=2-4\times10^{-4}$ T
Axial magnetic field	$B_0=90$ G
Plasma density	$n_e=1-4\times10^{10}$ cm^{-3}
Plasma electron temperature	$kT_e=0.2-0.5$ eV
Beam voltage	$V_b=50-200$ V
Beam current	$i_b=0.1-2$ A
Beam radius	$r_b=0.5-1$ cm
Beam pulse width	$t_b>500$ ns
Beam Larmor radius	$r_{Lb}\approx0.5$ cm
Beam rise time	$t_r\approx20$ ns$\leqslant50f_{pe}^{-1}$
Beam-to-plasma density ratio	$n_b/n_e=1\%-10\%$
Beam wavelength	$\lambda_b(v_bf_{pe}^{-1})=0.2-0.8$ cm
Electron plasma frequency	$f_{pe}=1-2$ GHz
Ion plasma frequency	$f_{pi}=3-7$ MHz
Cyclotron frequency	$f_{ce}=0.25$ GHz
Debye length	$\lambda_d<2\times10^{-3}$ cm
Ionization mean-free path	$L_{en}\approx200$ cm
Elastic scattering mean-free path	$\lambda_{en}>100$ cm

using shunt resistors to improve the sharpness of the beam front. Langmuir probes measure the plasma density and temperature with the beam turned off. An optical probe is used to measure the flux of beam and energetic electrons, and radio-frequency (RF) antennas are used to measure electrostatic waves generated in the plasma. The experiment is repetitively pulsed under reproducible conditions so that diagnostic signals may be statistically averaged to reduce noise (typically 500 shots per average). Also axial measurements are made by moving the diagnostic probes over many axial steps.

The optical probe consists of a lens in vacuum (linked via fiber optics to a photomultiplier tube sensitive in the visible spectrum) that collects light radially across the beam path. The detected light is caused by electron impact collisional excitation of background neutrals and ions. The minimum energy for exciting argon atoms is 10–15 eV and the excitation transition times are less than 10 ns. The total (visible) excitation cross section versus beam energies up to 200 eV has a profile[5] that rises sharply between 20 to 70 eV, peaks at 100 eV, and levels off. This novel optical diagnostics for measuring beam and tail electrons is completely nonperturbing, and gives excellent temporal and axial resolution ($\Delta t<5$ ns, $\Delta z<2$ mm).

The RF antenna consists of a semirigid ceramic-filled coaxial cable with the center wire exposed ~1 mm. Two antennas with RF mixers (2–8 GHz) are used to obtain the frequency, wavelength, phase velocity, and propagation direction of electrostatic waves in the plasma. A phase-lock conditional averaging technique[13] is used to obtain the measurements. A digital oscilloscope (LeCroy 7200) is configured to conditionally average only those wave signals whose initial phase lies within a narrow phase window. The resulting waveform measures the ensemble-averaged frequency and temporal coherence of the wave. Similarly, conditional triggering on a fixed reference antenna with signal averaging on a swept probe antenna is used to obtain the ensemble-averaged wavelength and phase velocity of the wave.

The basic experimental and physical parameters are listed in Table I. The rise time of the beam front relative to the electron plasma period is fast ($t_r/\tau_{pe}\leqslant50$) compared to previous experimental beam–plasma studies. More importantly, the ion plasma frequency f_{pi} is so low that only one ion oscillation ($\tau_{pi}\approx200$ ns) takes place during the entire beam–plasma interaction. This shows that ion processes cannot play a significant role in this experiment. The plasma frequency f_{pe} is 5–10 times the cyclotron frequency f_{ce}; therefore, cyclotron effects on plasma waves are minimal, i.e., the upper hybrid frequency $f_{\mathrm{UH}}\approx f_{pe}$. Finally, ionization and elastic scattering of the beam electrons do not contribute significantly to beam scattering, since the observed beam–plasma interactions occur only 5–10 cm away from the beam cathode.

III. OPTICAL MEASUREMENTS

A. Excitation light normalized to beam current

It is instructive to examine the scaling of excitation light with beam current, since the optical measurements are shown normalized to beam current and nonlinear scaling features will be used to indicate the occurrence of beam scattering and energetic tail production. The light intensity I_L emitted in perpendicular directions by neutrals and ions excited by an electron beam of density n_b, moving at velocity v_b at an angle θ with respect to an axial magnetic field is given by

$$I_L\propto(n_bv_b)(\sigma_in_e+\sigma_0n_0)/\cos\theta, \tag{1}$$

where σ is the excitation cross section and the subscripts i and 0 refer to ions and neutrals, respectively. The cosine term in the denominator accounts for the increase that results when beam electrons gyrates about the magnetic axis. A gyrating beam produces the same rate of collisional excitations as a parallel beam of the same energy, but since it is moving slower in the axial direction, the light produced that is detected by a probe of fixed axial width is greater. Dividing through by the beam current i_b gives the normalized light intensity I_N, which is a measure of the total light that results from each injected beam electron and is given by

$$I_N=I_L/i_b=K(\sigma_in_e+\sigma_0n_0)/\cos\theta, \tag{2}$$

where K is a constant that incorporates the physical constants and geometrical factors, e.g., the solid angle of the optical probe. The plasma is sufficiently optically thin, such that self-absorption of beam excitation light is negligible.

For a beam injected along the axis $\theta_i=0$, I_N is constant along the beam path for very low i_b in the limit of single particle behavior with no beam–plasma interactions. However, I_N is also fairly constant for beam–plasma interactions that result in purely axial acceleration or deceleration of the beam electrons, e.g., from axial sheaths, double layers, or parallel wave trapping. Since $\theta_f=0$ and the beam flux is unchanged ($n_f v_f = n_i v_i$), I_N changes only from the excitation cross section, which is, generally, weakly dependent on v_b. Therefore, in beam–plasma processes that change only the parallel energy of the beam electrons, I_N is roughly constant along the beam trajectory and for varying beam current.

In contrast, interactions that scatter beam electrons elastically into perpendicular direction will increase I_N, since $\cos\theta_f$ is less than unity, even though the axial beam flux remains unchanged. For example, I_N doubles if all the beam electrons are scattered to 60°. Also, I_N will increase due to the production of energetic electron tails accelerated from the background plasma. If one beam electron is replaced by several tail electrons totaling the same energy, I_N doubles for 50 eV tail electrons. However, I_N will not increase as much for lower tail energies, since the excitation cross sections fall quicker than the increase in tail electron flux that is given by conservation of beam energy. An important but subtle enhancement mechanism is the transient buildup in the population of scattered beam or tail electrons. This causes I_N to increase until the production of these secondary electrons is balanced by the free-streaming of these electrons out of the detection region. The initial buildup time for I_N will, therefore, depend on the velocity of the secondary electrons and the axial width of the optical probe.

B. Observation of beam scattering and energetic tail electrons

The basic dependence of excitation light versus beam current for fixed axial position is shown next. In Fig. 2(a), I_L increases continuously with i_b, but after normalization to beam current in Fig. 2(b), I_N scales linearly only for $i_b<0.3$ A and increases up to four times the linear level at large i_b. The nonlinearity in I_N is conclusive evidence of the presence of beam scattering and energetic tail electrons. This profile of I_N vs i_b (or n_b), which starts at unity and increases nonlinearly, is consistent with the growth rate $\gamma/\omega_{pe} \propto (n_b/n_e)^{1/3}$ for the streaming beam–plasma instability.[14]

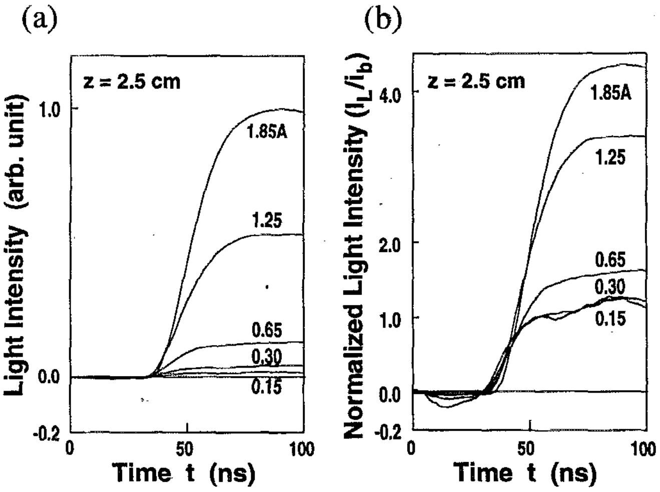

FIG. 2. Excitation light intensity for different beam currents, taken during the beam front at fixed probe position, scaled as (a) intensity and (b) intensity normalized to beam current. The nonlinear light intensities indicate the occurrence of beam scattering and energetic electron tail production.

It is possible to distinguish between beam scattering and energetic tail production during the initial transition from single particle propagation to strong beam–plasma interactions. Figure 3 shows the onset of nonlinear I_N for increasing i_b at fixed z and for increasing z at fixed i_b. The traces are shifted in time to a common front onset (marked by down arrow) and vertically offset for clarity. The turning region between the light front and plateau (marked by up arrows) is used to define the end of the front. The width of the front is given by the time difference between the up and down arrows. The similarity in the transition between increasing beam current in Fig. 3(a) and axial position in Fig. 3(b) is indicative of a convective beam instability whose growth rate is proportional to the beam density, i.e., increasing i_b is equivalent to moving to farther z to obtain the same absolute growth in the instability. Initially, the front increases only slightly in height and width ($i_b=0.65$ A or $z=3$ cm), then doubles in both height and width ($i_b=1.25$ A or $z=4.5$ cm). The large change between the top and middle traces indicates the different buildup times and steady-state populations of the scattered beam and tail electrons, in addition to the occurrence of perpendicular motions in the secondary electrons. Since the tail electrons move much slower axially than the beam electrons, their buildup time can be much longer than the front width of the beam. From the data in Fig. 3, I_N

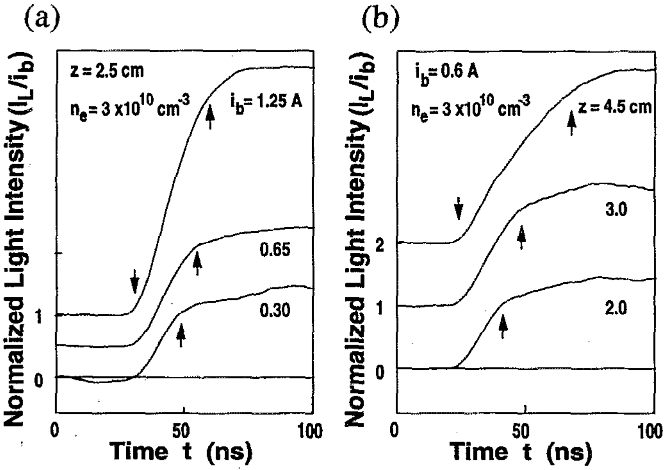

FIG. 3. Transition in normalized light intensity from single particle to nonlinear levels, by (a) increasing the beam current at fixed axial position and (b) increasing the axial distance at fixed beam current. The down arrow marks the onset of the front, and the up arrow points to the turning region between the front and plateau.

increases up to 50% from beam scattering and 100%–200% from energetic tail electron production. Unfortunately, the exact density and energy distribution of the scattered beam and tail electrons cannot be obtained from the light measurements. At later times, the individual contributions from the injected beam, beam scattering, and electron tails completely merge and are inseparable; I_N becomes simply a qualitative measure of the total beam–plasma particle interaction in comparison to single particle behavior, integrating beam scattering, energetic tail production, and heating of the background plasma.

C. Axial propagation and erosion of the beam front

The axial propagation of the beam front is also strongly modified by the beam–plasma particle interactions described previously. In particular, the injected cold beam front can erode during propagation and evolve into a warm front that propagate much slower than its injected speed. The propagation curve of the front for single particle behavior is determined next, which includes the effects of a finite rise time in the beam voltage. For the beam risetimes (t_r<20 ns) and axial distances (z<10 cm) used in this experiment, one observes the front moving slower at first, because electrons are injected at lower speed during the initial ramping of the beam voltage. After some finite time and distance, the front propagates at the final beam speed, when electrons injected at the final beam voltage catch up and overtake the earlier injected electrons. Our single particle model considers a beam voltage ramp that injects electrons with an initial velocity v_i at time $t=0$ and linearly ramps up to a final beam velocity v_b at $t=t_r$. A nonzero v_i is used, since a minimum beam energy is needed to produce excitation light. The effective v_i will depend on the risetime of the beam current and the excitation cross-section profile. The acceleration region for the electrons is assumed to be negligibly short and the position of the front z_f is given by the position of the electrons that have moved farthest away at any given time t. This produces the following solution, which consists of three continuous lines:

$$\begin{aligned} z_f&=v_i t, \quad 0<t<t_i, \quad a=\frac{(v_b-v_i)}{t_r},\\ z_f&=\frac{a}{4}\left(t+\frac{v_i}{a}\right)^2, \quad t_i<t<t_b, \quad t_i=\frac{v_i}{a}, \qquad (3)\\ z_f&=v_b(t-t_r), \quad t_b<t, \quad t_b=t_r+\frac{v_b}{a}. \end{aligned}$$

The axial propagation of the light front from an electron beam injected into the plasma is shown in Fig. 4, for several i_b. Each plot is a set of normalized light intensity traces taken from z=2.5 to 32.5 cm at 5 cm intervals, vertically offset for clarity. The top set (i_b=0.3 A) is closest to single particle propagation, with I_N roughly unity. The middle and bottom sets (i_b=1.3 and 2 A) are very nonlinear with I_N up to 3 times the linear level. Note that the qualitative shapes of the light fronts versus axial position are similar for the three sets, except for quantitative differences in the normalized intensity and front width. It would be easy to misinterpret the behavior of the beam fronts as single particle propagation in experimental studies where scaling measurements to beam current are not possible or ignored.

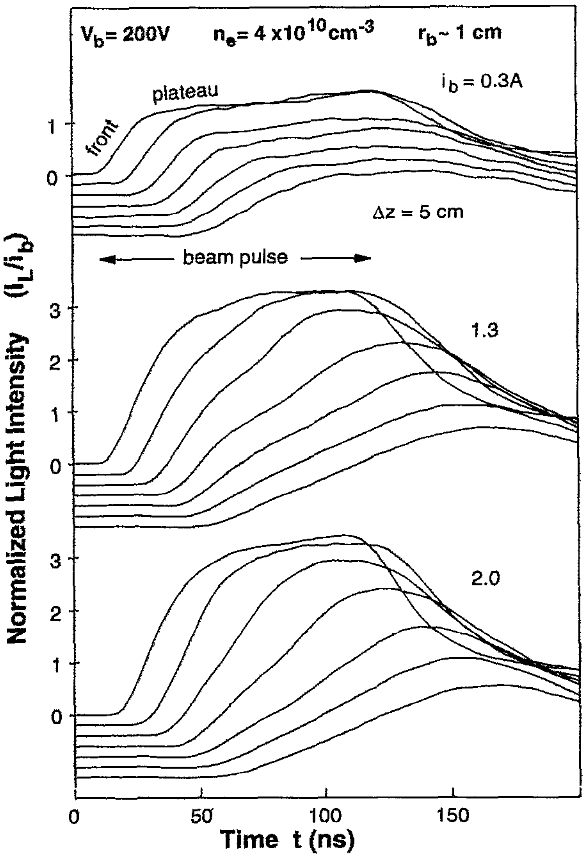

FIG. 4. Axial propagation of the light front for different beam currents. Each plot is a set of normalized light intensity traces taken from 2.5 to 32.5 cm away from the beam cathode at 5 cm intervals.

The propagation of the beam fronts in Fig. 4 follows the single particle solution given by Eq. (3) only at the onset time t_{ON} of the front, which is defined by the intersection of the baseline and the initial slope of the front. The bulk of the light front, e.g., half-height of front or turning region near plateau, propagates much slower than the single particle curve. Figure 5 shows the propagation curve of t_{ON} for i_b=0.3 and 1.3 A, compared with the theoretical curve in Eq. (3), using v_i=90 V, v_b=250 V, and t_r=10 ns for the best fit to the data points. The match between the experimental data and theory is very good, including the effects of the finite voltage ramp. The initial speed v_i may be higher than expected; however, the beam voltage at the effective onset of the beam current cannot be measured accurately for a direct comparison. The final speed v_b is higher than the applied beam voltage of 200 V and probably indicates that some beam electrons have been accelerated by the beam–plasma instability.

The axial profile of I_N at the beam front also deviates significantly from single particle behavior, with the initial beam front eroding during propagation into the plasma. The turning region between the front and plateau should not be

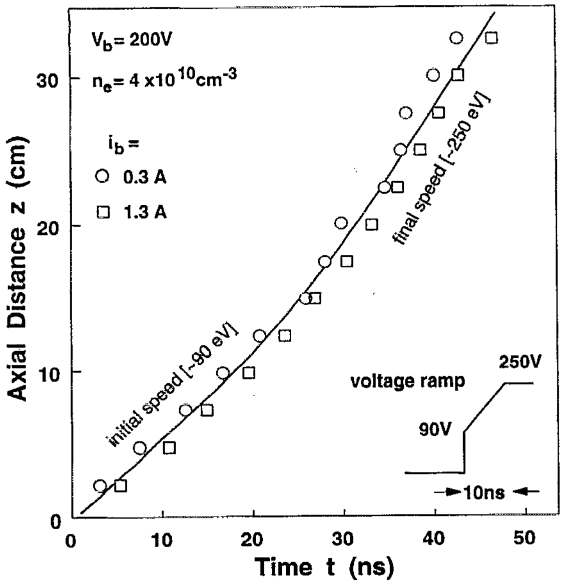

FIG. 5. Axial propagation curve at the onset of the front, compared to single particle propagation given by Eq. (3). The inset shows the parameters of the voltage ramp used in the theoretical curve.

used to define the front position, because of nonlinear modifications due to beam scattering and energetic tail production during propagation. Instead, we choose a front time t_f that is defined by the single particle propagation curve for t_{ON}, using Eq. (3) with $v_i=90$ V, $v_b=200$ V, and $t_r=10$ ns, plus an added shift of 15 ns for the front width (based on Fig. 4: $i_b=0.3$ A, $z=2.5$ cm). The axial profiles $I_N(z,t_f)$ are shown in Fig. 6 for several i_b. Ideal single particle propagation should give a flat axial profile of unity. Since the profile for $i_b=0.3$ A drops steadily, it is still far from the single particle limit. The axial profiles for $i_b=1.3$ and 2.0 A reach nonlinear levels already at $z=2.5$ cm, which indicates that beam scattering and energetic tail production can begin within the risetime of the beam front. Moreover, $I_N(z,t_f)$ falls rapidly below unity, showing that the injected beam front erodes with axial distance. Finally, the absence of a distinct front or step that moves ahead at the injected beam speed in the data in Fig. 4 is further confirmation of erosion in the beam front.

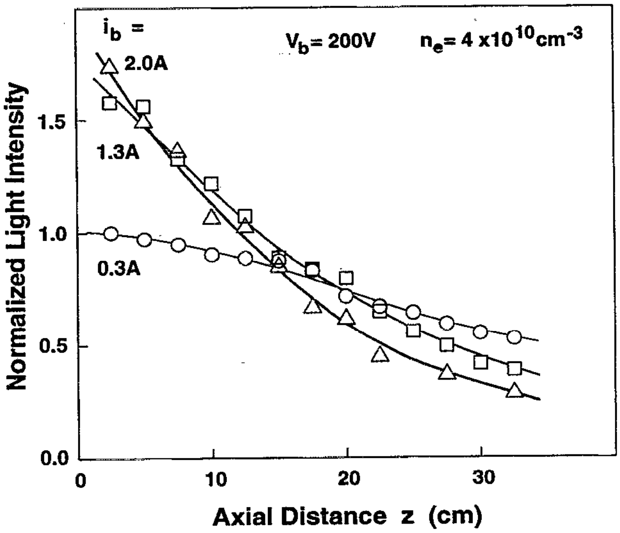

FIG. 6. Axial profile of the normalized light intensity at the beam front for the data in Fig. 4, which shows the erosion in the beam front during beam propagation. A single particle propagation curve is used to define in time the front of the beam at different axial distances.

The optical measurements presented clearly indicate that beam scattering and energetic tail production can occur at the beam front during the injection of an electron beam into a background plasma without significant contribution from ion dynamics. In addition, the injected beam front can erode rapidly, resulting in a heated electron front that propagates significantly slower than the injected beam particle speed.

IV. ELECTROSTATIC WAVE MEASUREMENTS

A. High-frequency (HF) ballistic beam mode and beam bunching

It is common to find in beam–plasma experiments electrostatic waves that are excited near the electron plasma frequency due to the streaming beam–plasma instability. Linear analysis of the beam–plasma dispersion relation[14] for weak beams ($n_b/n_e \ll 1$) shows that the strongest coupling occurs at the resonance condition where the phase velocity of the plasma wave matches the beam speed $\omega - k v_b = 0$. However, a beam bunched by the same beam–plasma instability can ballistically generate high-frequency (HF) electrostatic signals on an antenna that are identical to the plasma wave. In addition, if the beam bunching becomes nonlinear or nonsinusoidal, then ballistic modes at harmonics of f_{pe} are generated that all propagate at the beam speed. In contrast, the Bohm–Gross plasma wave $\omega^2 = \omega_p^2 + 3k^2 v_{\mathrm{th}}^2$ is not driven unstable by the beam at the harmonics of f_{pe}, since a resonance condition is no longer present, and is also strongly Landau damped ($\lambda \leq \lambda_D$) at these frequencies.

Electrostatic waves are detected by RF antennas inside the beam flux tube during beam injection at the plasma frequency and its harmonics that are extremely monochromatic and coherent for over a hundred oscillations. The typical wave measurement is shown in Fig. 7(a) and consists of a set of phase-lock averaged traces taken from $z=1.15$ to 2.2 cm at 1.5 mm intervals, vertically offset for clarity. The local oscillator frequency f_{LO} is at 2.25 GHz and set below the wave frequency f_{HF}. On the right is the axial profile of the normalized peak wave intensity and in Fig. 7(b) is the axial propagation of the phase maxima and minima. The axial distance between the phase peaks at a fixed time gives the wavelength λ. The wave frequency is given by $f_{\mathrm{HF}} = f_{\mathrm{LO}} + 1/\tau_M$, where τ_M is the period of the frequency-mixed wave. The coherence time is roughly 40 ns, which corresponds to about 100 wave periods. Finally, the phase velocity $v_\phi = f\lambda$ roughly matches the beam speed to within experimental errors.

The harmonic properties of the high-frequency wave mode are shown in Fig. 8. A family of harmonic frequency peaks is detected by scanning f_{LO} from 2–8 GHz. The plot of frequency versus harmonic number is very linear and crosses the origin. The fundamental frequency f_1 agrees well with f_{pe}, which is measured independently with a Langmuir

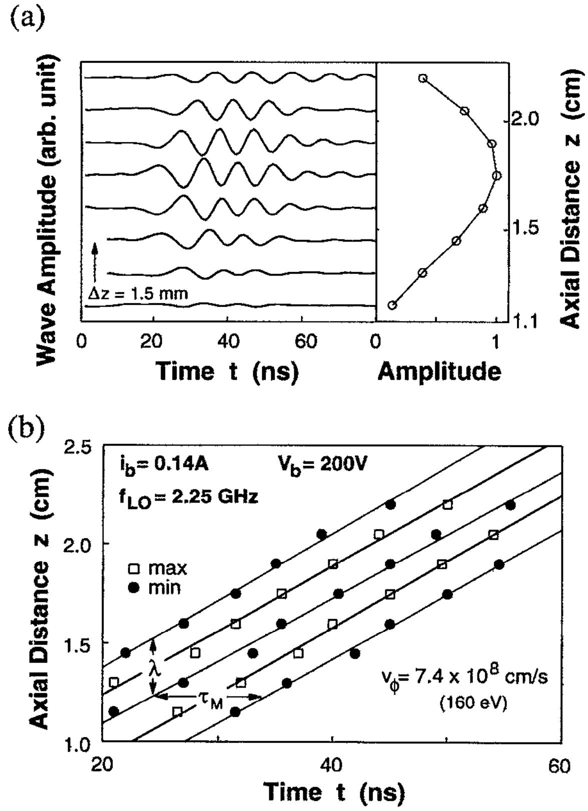

FIG. 7. HF ballistic beam mode measurement: (a) phase-lock averaged signal for different axial distances, with normalized peak amplitude on the right, and (b) propagation of the phase maxima and minima, which gives the frequency and wavelength of the wave.

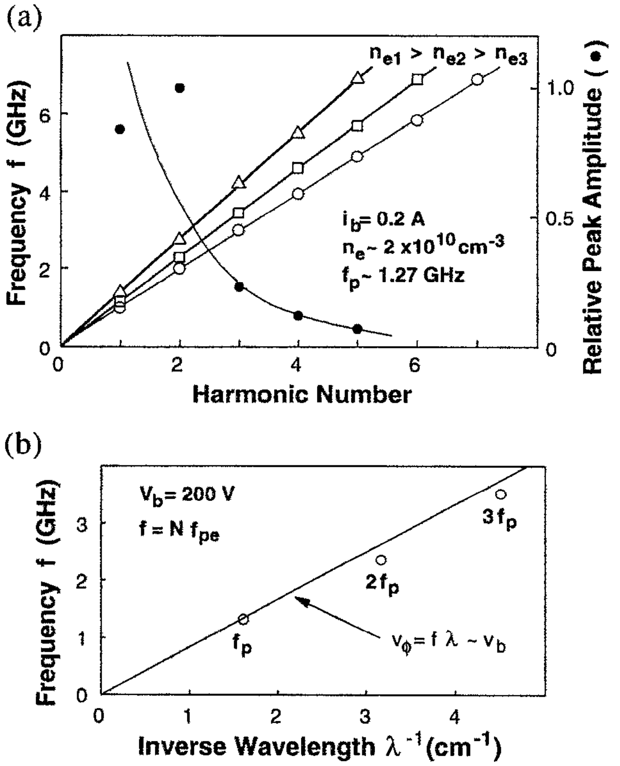

FIG. 8. Harmonic features of HF mode: (a) families of harmonic frequencies for different plasma densities and (b) inverse wavelengths and phase velocities for several harmonics. These features indicate the ballistic nature of the mode and the occurrence of strong beam bunching.

probe. The profile of normalized peak wave amplitude versus the harmonic number is shown by the solid circles, and does not vary much with i_b or n_e. The phase velocity for first three harmonics are plotted in Fig. 8(b) and they are all close to the injected beam speed. This result that the harmonic modes all propagate at the beam speed indicates that the detected HF wave is a ballistic beam mode, instead of a plasma wave. In addition, the detection of high harmonic numbers shows that the beam is severely bunched by the beam–plasma instability.

B. Correlation of collapse in ballistic mode with beam scattering

In single-shot concurrent optical and electrostatic wave measurements, a direct correlation between the onset of beam scattering and collapse of the coherent ballistic mode into broadband turbulence is observed, both versus beam current and axial probe position. Figure 9 shows the axial correlations between the light front, the HF ballistic mode at the second harmonic and a new lower-frequency (LF) electrostatic wave (described in the next section). At $z=2$ cm, although both HF and LF wave signals are large and coherent, the light intensity at the front is still at the linear level. This shows that the beam bunching alone does not enhance the light intensity and supports the previous optical inferences that axial bunching with change solely in the parallel energies of the electrons does not produce much increase in light. In contrast at $z=4$ cm, the HF mode has collapsed and become more broadband, which coincides with when the light front becomes nonlinear. This correlation of nonlinear light with the breakup of the ballistic wave complements the optical results that enhanced light intensities indicate perpendicular electron motions, since collapse in the beam bunching must lead to beam scattering and random perpendicular beam electron trajectories. It is likely that the plasma wave generated by the beam–plasma instability also becomes turbulent during the collapse, producing random radial electric fields, however our wave diagnostics cannot cleanly separated the plasma wave from the fundamental mode of the ballistic wave.

These scattering and bunching results are unique to the beam front or short pulse environment, and are absent under steady-state beam–plasma conditions, shown in concurrent measurements for a double pulse beam injection in Fig. 10. The beam voltage and current waveforms are nearly identical for both pulses (not shown). However, beam bunching does not occur during the second pulse and because of this absence, the second light front exhibits much less scattering than the first light pulse and is closer to single particle behavior. The presence of energetic tail electrons and a heated background plasma with some limited ion motions suppress the reoccurrence of strong beam bunching and beam scattering during the second pulse.

A rough measurement of the plasma potential has been

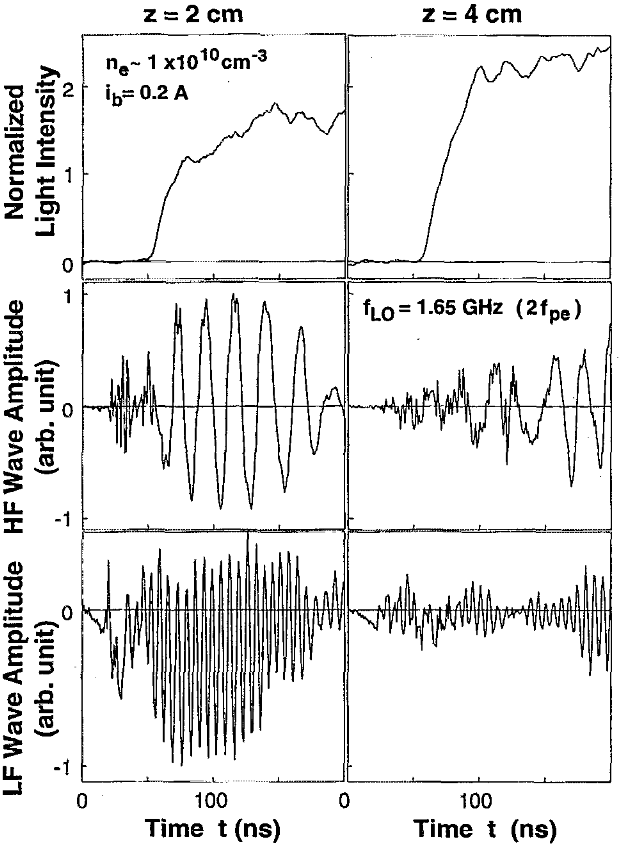

FIG. 9. Concurrent measurements of the light front, HF ballistic mode and LF wave at two axial positions, which show the correlation between collapse in beam bunching and beam scattering.

made to check whether large potential gradients are produced during beam injection. The measurement is done by biasing the axial antenna negatively to -9 V to collect background electrons and using a low-pass filter to remove the superimposed LF wave. The probe signal at several axial positions is shown in Fig. 11 and reveals a negative potential well of only -5 to -10 V, located between $z=1$–4 cm at $t=100$–150 ns. Note that the potential well also collapses when the light front becomes nonlinear (compare Figs. 9 and 11). Biasing the antenna further to -30 V repels all the background electrons and reduces the probe current to zero. This verifies that in this experiment, there are no large potential gradients capable of significantly retarding the injected beam.

C. LF electrostatic wave

The LF wave shown earlier has a frequency ($f_{\rm LF}$=50–400 MHz) that lies between f_{pe} and f_{pi}, and can be below or above the electron cyclotron frequency f_{ce}. The LF wave is measured using the same antenna setup as for the HF wave, except the signal is phase-lock averaged directly without frequency mixing and the antenna is biased to -30 V to eliminate direct electron pickup on the antenna. A typical set of LF wave traces is shown in Fig. 12(a), taken from z=1.6 to 3.4 at 3 mm intervals. One additional trace at z=1.75 cm is included to clarify the direction of the phase propagation, which surprisingly is antiparallel to the direc-

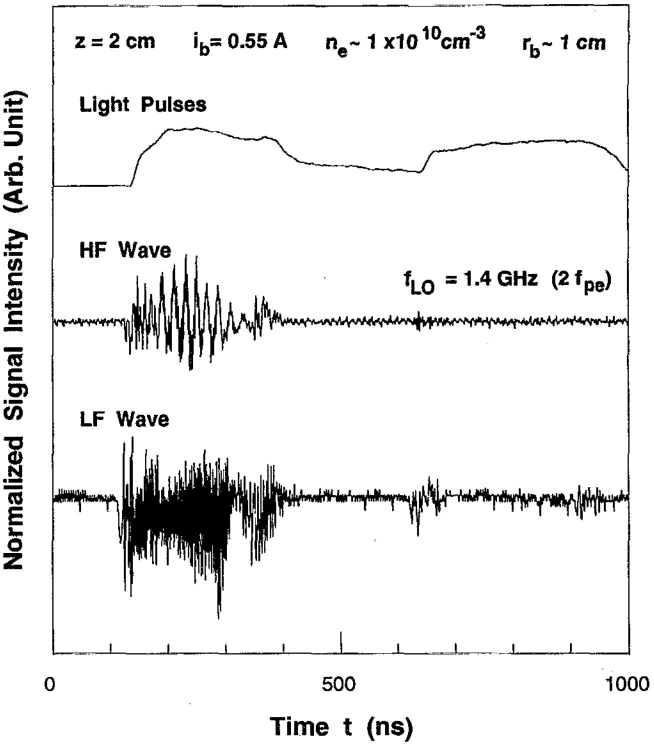

FIG. 10. Concurrent measurements of the light front, HF ballistic mode and LF wave near the beam cathode for a double pulse beam injection. The absence of coherent waves and nonlinear light intensities during the second pulse shows that beam bunching and beam scattering are unique to short beam pulses and not found under steady-state beam–plasma conditions.

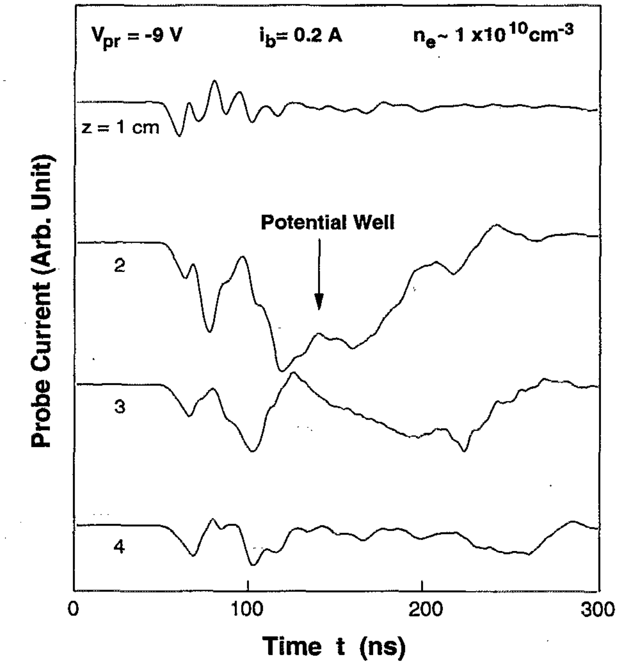

FIG. 11. Small negative potential well detected with an antenna biased to -9 V and low-pass filtering, which shows the absence of large potential fields capable of retarding the injected beam.

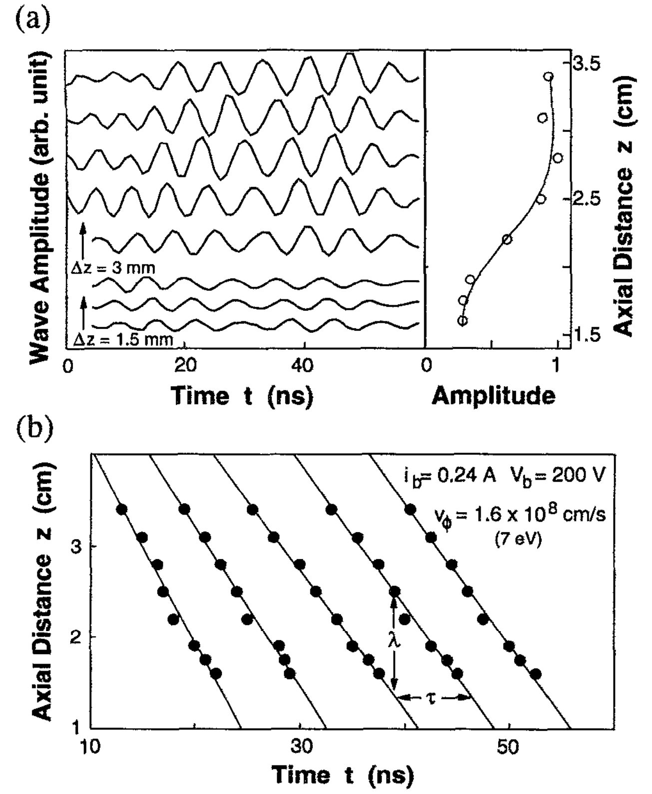

FIG. 12. LF wave measurement: (a) phased-lock averaged wave signal for different axial distances, with normalized peak amplitude on the right, and (b) propagation of the phase maxima, from which the frequency and wavelength of the wave are obtained.

tion of beam propagation. Analysis of the propagation of the phase maxima in Fig. 12(b) obtains the ensemble-averaged frequency, wavelength, and phase velocity for the LF wave mode. In this case, λ is roughly 1 cm and v_ϕ is much lower than v_b.

Figure 13(a) shows that f_{LF} is very sensitive to the afterglow time t_{AG}, which sets the plasma density n_e and temperature kT_e. While n_e is obtained from the fundamental frequency of the ballistic mode ($f_{pe} \approx f_{\mathrm{HF}}$), kT_e is not measured, since Langmuir probes are difficult to interpret during beam injection. Also the beam current is kept constant, however f_{LF} varies by an order of magnitude, while n_e changes only by a factor of 3. It may be that a tail electron population, which is not being measured, is responsible for the sensitive scaling of f_{LF} with t_{AG}. The frequency versus inverse wavelength are shown for several t_{AG} in Fig. 13(b), with the corresponding phase velocity versus relative beam density displayed in Fig. 13(c), labeled in terms of the energy of an electron moving at a speed equal to v_ϕ. At the onset of the LF wave, $f_{\mathrm{LF}} \approx 50$ MHz and $1/2 m v_\phi^2 \approx 0.5$ eV. Therefore, the phase velocity cuts off close to the electron thermal velocity given by kT_e of the unheated plasma. Finally, the LF wave forms beat waves, shown in Fig. 14, with the corresponding multiple peak spectra displayed below, obtained from FFT analysis. However, the LF wave does not appear to form standing waves.

There are several known wave modes that lie between

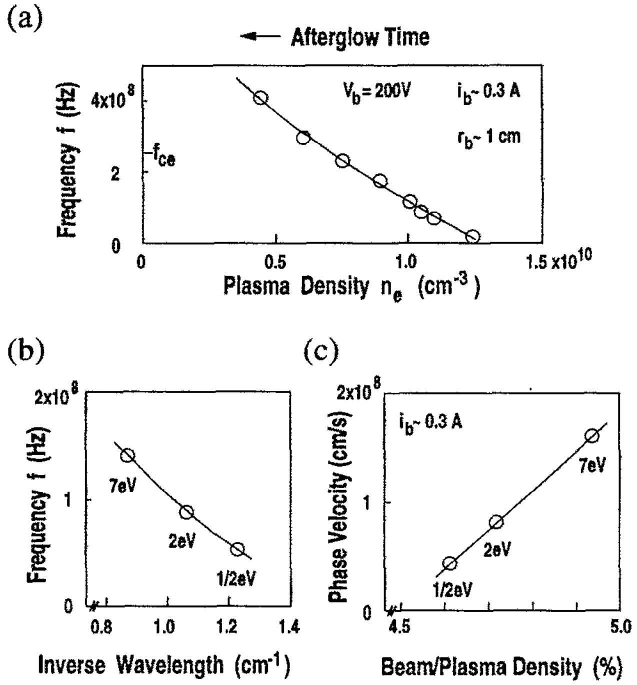

FIG. 13. Dependence of LF wave on plasma density: (a) frequency versus plasma density, (b) frequency versus inverse wavelength, and (c) phase velocity versus relative beam density. The labels in eV are in terms of the kinetic energy of an electron that is moving at the phase velocity of the wave.

f_{pe} and f_{pi}. The Buneman instability[15] gives both frequency $f \approx 1/2 (f_{pe} f_{pi}^2)^{1/3} [\sim 10 \text{ MHz}]$ and wavelength $\lambda \approx \lambda_D$ that are much lower than our measured values. The electron acoustic frequency for a two-electron-temperature plasma[16] falls into the observed range of values. However, neither the temperature nor the density of the inferred electron tail population can be estimated or measured, therefore comparison with theory is not feasible. A final possibility is a cylindrical plasma waveguide mode, similar to the Gould–Trivelpiece mode,[17] which supports backward waves. The small negative potential well could produce a radial low-density electron plasma channel inside the background plasma, setting up a finite geometry configuration in which the beam wavelength $\lambda_b = v_b / f_{pe}$ approaches the radial dimension of the electron plasma channel. Overall, a satisfactory identification and understanding of the LF mode remains to be found.

The wave measurements presented indicate that the injected beam bunches strongly due to the beam–plasma instability and collapses into broadband turbulence, which corroborates well with the optical measurements of beam scattering and plasma heating. A LF wave is also detected that is probably important for the scattering process of the beam.

V. CONCLUSIONS

In this experimental study, the particle and wave interactions at the front of an electron beam injected into a background plasma have been measured carefully using novel optical and antenna diagnostics. The beam is observed to

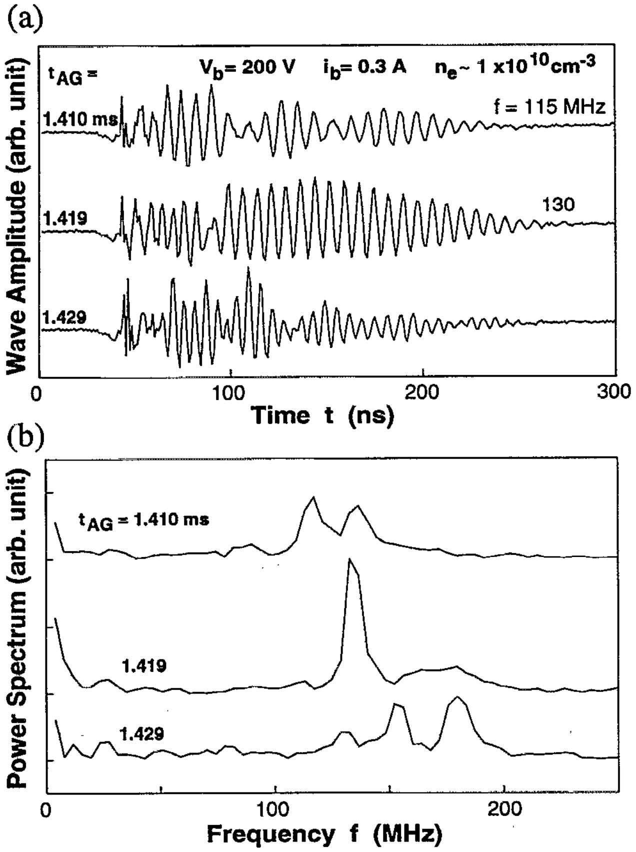

FIG. 14. Beat phenomena in the LF wave: (a) beat waves for several afterglow times and (b) corresponding frequency spectra from FFT analysis.

bunch along the axial direction due to the streaming beam–plasma instability, and then scatter into perpendicular directions, accompanied by the production of energetic tail electrons and plasma heating. The injected beam front erodes during propagation and evolves into a warm front that moves much slower than the injected beam speed. A LF wave is also detected during beam injection that is coupled to the scattering interactions; however, its exact role and identity is not completely resolved.

These beam–plasma interactions occur rapidly on time scales during which the plasma ions are essentially immobile, and therefore, dominated by the electron dynamics, and electrostatic waves or potentials. Moreover, these results are unique to short beam injections and absent under steady-state beam–plasma conditions. Previous investigations use Langmuir wave collapse or ion wave scattering to explain the occurrence of beam scattering and energetic tail production, which our observations show can occur without ion dynamics. Current plasma theory does not adequately explain such a beam–plasma regime. Finally, in our experiment, the detailed mechanisms involved in the transitions from beam bunching to beam scattering and energetic tail production to plasma turbulence are not completely resolved, and may require future development of diagnostics that can time resolve the plasma density and plasma potential on the time scale of the beam front, and separate plasma wave turbulence from collapse in the ballistic beam mode.

ACKNOWLEDGMENTS

The authors would like to thank Dr. J. M. Dawson, Dr. M. Ashour-Abdalla, Dr. F. Chen, Dr. C. Joshi, and Dr. J. M. Urrutia for many useful discussions during the course of this work.

This work was supported in part by National Science Foundation (PHY and ATM divisions) and National Aeronautics and Space Administration Grants.

[1] J. R. Winckler, Rev. Geophys. Space Phys. **18**, 659 (1980).
[2] G. V. Rao and S. K. Iyyengar, J. Appl. Phys. **71**, 2503 (1992).
[3] W. W. Destler, P. G. O'Shea, and M. Reiser, Phys. Fluids **27**, 1897 (1984).
[4] J. B. Rosenzweig, P. Schoessow, B. Cole, C. Ho, W. Gai, R. Konecny, S. Mtingwa, J. Norem, M. Rosing, and J. Simpson, Phys. Fluids B **2**, 1376 (1990).
[5] L. Y. Chan and R. L. Stenzel, Phys. Rev. Lett. **67**, 2147 (1991).
[6] D. A. Whelan and R. L. Stenzel, Phys. Fluids **28**, 958 (1985).
[7] J. A. Michel and J. P. Hogge, Rev. Sci. Instrum. **60**, 33 (1989).
[8] N. Singh and R. W. Schunk, Plasma Phys. Controlled Fusion **26**, 859 (1984).
[9] M. M. Shoucri and L. R. O. Storey, Phys. Fluids **29**, 262 (1985).
[10] P. L. Prtichett and R. M. Winglee, J. Geophys. Res. **92**, 7673 (1987).
[11] P. V. Vedenin, V. G. Rukhlin, and V. P. Tarakanov, Sov. J. Plasma Phys. **15**, 724 (1989).
[12] R. Bonifacio, C. Maroli, and N. Piovella, Phys. Rev. Lett. **69**, 3177 (1992).
[13] H. Johnsen, H. L. Pecseli, and J. Trulsen, Phys. Fluids **30**, 2239 (1987).
[14] R. J. Briggs, *Electron-Stream Interaction with Plasmas* (MIT Press, Cambridge, MA, 1964).
[15] O. Buneman, Phys. Rev. **115**, 503 (1959).
[16] S. Peter and R. L. Tokar, Phys. Fluids **28**, 2439 (1985).
[17] A. W. Trivelpiece and R. W. Gould, J. Appl. Phys. **30**, 1784 (1959).